JACS
JOURNAL OF THE AMERICAN CHEMICAL SOCIETY
pubs.acs.org/JACS
Article

Aliovalent Substitution Tunes Physical Properties in a Conductive Bis(dithiolene) Two-Dimensional Metal−Organic Framework

Lei Wang, Andrea Daru, Bhavnesh Jangid, Jie-Hao Chen, Ningxin Jiang, Shrayesh N. Patel, Laura Gagliardi, and John S. Anderson*

Cite This: J. Am. Chem. Soc. 2024, 146, 12063−12073

ABSTRACT: Two-dimensional conductive metal−organic frameworks have emerged as promising electronic materials for applications in (opto)electronic, thermoelectric, magnetic, electrocatalytic, and energy storage devices. Many bottom-up or postsynthetic protocols have been developed to isolate these materials or further modulate their electronic properties. However, some methodologies commonly used in classic semiconductors, notably, aliovalent substitution, are conspicuously absent. Here, we demonstrate how aliovalent Fe(III) to Ni(II) substitution enables the isolation of a Ni bis(dithiolene) material from a previously reported Fe analogue. Detailed characterization supports the idea that aliovalent substitution of Fe(III) to Ni(II) results in an in situ oxidation of the organic dithiolene linker. This substitution-induced redox tuning modulates the electronic properties in the system, leading to higher electrical conductivity and Hall mobility but slightly lower carrier densities and weaker antiferromagnetic interactions. Moreover, this aliovalent substitution improves the material's electrochemical stability and thus enables pseudocapacitive behavior in the Ni material. These results demonstrate how classic aliovalent substitution strategies in semiconductors can also be leveraged in conductive MOFs and add further support to this class of compounds as emerging electronic materials.

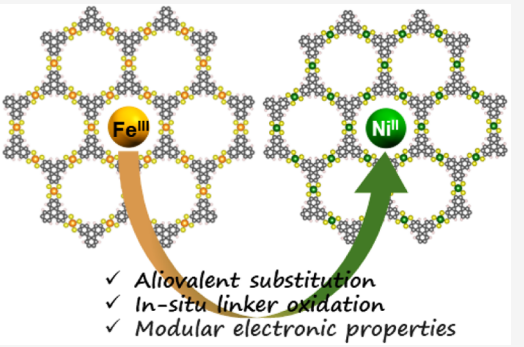

INTRODUCTION

Two-dimensional conductive metal−organic frameworks (2D c-MOFs) have emerged as a new class of electronic materials with tunable charge transport behavior that coexists with structural rigidity, chemical flexibility, and intrinsic porosity.[1,2] These features make them uniquely suited for applications in (opto)electronic, thermoelectric, magnetic, electrocatalytic, and energy storage devices.[3−8] Electrical conductivity in these materials is enabled by charge transport pathways including redox hopping, through-space, through-bond, or band-like transport.[9] Many bottom-up and postsynthetic approaches have been developed to design these electrically conductive MOFs, including using sulfur-containing ligands for improved energy matching, extending π−d conjugation for efficient delocalization, building continuous π−π interactions in space, and integration of redox-active guests to promote charge hopping.[10] Among this family, stacked 2D c-MOFs with extended π-conjugation and out-of-plane π−π stacking interactions are particularly modular platforms for conductive materials.

In addition to the geometric structure of 2D c-MOFs, the exact redox-state of the linker and metal centers is vitally important for bulk charge transport properties.[11] This feature provides an additional programming point for the synthesis and tuning of 2D c-MOFs through redox chemistry.[12,13] Triphenylene-based linkers with ortho-substituted ligating atoms (N, O, and S) have been one of the most investigated motifs in the synthesis of 2D c-MOFs.[14] In addition to d−π bond covalency provided by these planar linkers, their redox-noninnocence can engender *in situ* redox modulation during synthesis as well as via postsynthetic redox tuning.[2,9] This is particularly true for triphenylenehexathiol (THT)-based linkers; several THT-based 2D c-MOFs have been reported with high conductivity, charge mobility, and tunable charge transport.[15−17]

Previously, we have reported electronic tuning of the organic linker over four distinct redox states in THT-based 2D c-MOFs featuring Fe bis(dithiolene) motifs.[18] Detailed spectroscopic measurements revealed that the redox-tuning of these materials occurs primarily on the THT linkers, in contrast to more commonly encountered metal-based redox events. The physical properties of these materials, such as their electrical conductivity, thermoelectric behavior, carrier concentration,

Received: February 5, 2024
Revised: April 2, 2024
Accepted: April 3, 2024
Published: April 18, 2024

https://doi.org/10.1021/jacs.4c01860
J. Am. Chem. Soc. 2024, 146, 12063−12073

and magnetic interactions, all respond dramatically to ligand-centered redox tuning, with a general trend of increasing conductivity with increasingly oxidized THT linkers. The most oxidized material in this series, $\mathbf{Fe_3(THT)_2}$ has Fe^{3+} centers with formally THT 4.5-linkers.

These results underscore how the porosity and redox activity of this class of MOFs make them unique electronic materials. However, it is notable that despite this modularity, classic strategies for tuning electronic properties in semiconducting materials have not been as widely employed in MOFs. For instance, a prototypical semiconducting material, Si, is classically tuned by incorporation of either group 13 or group 15 elements for p-type or n-type doping, respectively (Figure 1A). Furthermore, complete exchange of group 14 elements with pairs of group 12/16 or 13/15 elements generates new semiconducting materials.[19] This strategy, called aliovalent substitution, inherently relies on the different ionic charges between substituting elements to change physical properties including carrier densities and types (Figure 1B).[20,21] This is particularly important in nonporous solid-state semiconductors where formal oxidation and reduction of the material can be challenging due to difficulties with the incorporation of charge balancing ions without disruption of the periodic lattice. Despite this broad importance and precedent in solid-state chemistry, aliovalent substitution in c-MOFs has been only sparingly investigated. While a series of detailed and thorough studies on how isovalent substitutions (for instance substituting or alloying Co(II) for Ni(II) or Cu(II)) have been reported to tune properties in c-MOFs (Figure 1C), analogous studies with aliovalent substitutions are lacking.[22]

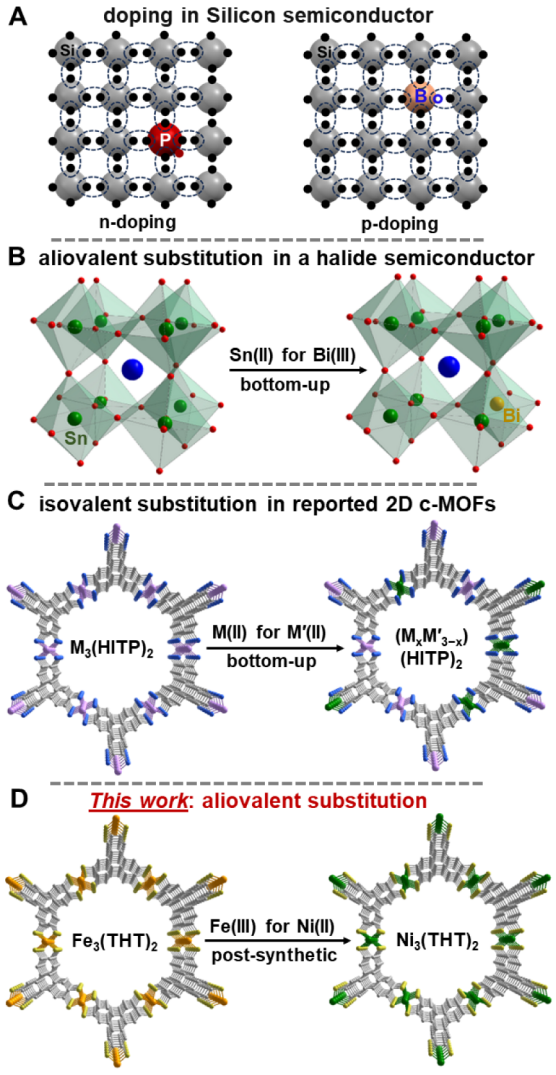

Figure 1. (A) Schematic description of doping in silicon. (B) An example of aliovalent substitution in the $CsSnBr_3$ semiconductor. Color code: blue, Cs; green, Sn; red, Br; yellow, Bi. (C) Schematic description of isovalent substitutions in a series of 2D c-MOFs. HITP: hexaiminotriphenylene. Color code: blue, N; gray, C; purple/green, Co or Cu or Ni. H is omitted. (D) Schematic description of the aliovalent substitutions in this work. THT: triphenylenehexathiol. Color code: orange, S; yellow, Fe; green, Ni; gray, C. H is omitted.

Here, we report how aliovalent substitution enables isolation of an MOF with oxidized formal THT^{3-} linkers (Figure 1D). We had previously noted that further chemical oxidation of $\mathbf{Fe_3(THT)_2}$ did not provide stable materials, and this prompted us to investigate alternative synthetic protocols to obtain more highly oxidized THT-based MOFs. Aliovalent substitution of Fe(III) to Ni(II) leads to in situ oxidation of the linker and stabilizes a higher linker oxidation state that is inaccessible with Fe alone. This aliovalent-substituted material exhibits higher electrical conductivity and mobility but a weaker antiferromagnetic coupling. Furthermore, transmetalation of Fe to Ni leads to improved electrochemical stability and thus enables pseudocapacitive behavior. These results show how aliovalent substitution can be a useful strategy in obtaining and tuning electrochemically active 2D metal–organic materials, in analogy with the long-standing use of this strategy in other semiconducting materials.

RESULTS AND DISCUSSION

Synthesis, Structure, and Component Redox States. The oxidized starting material for aliovalent substitution, $\mathbf{Fe_3(THT)_2}$, was synthesized following our previously reported method.[18] Freshly prepared $\mathbf{Fe_3(THT)_2}$ was then soaked in a 0.2 M $NiCl_2 \cdot 6H_2O$ solution in DMF at 70 °C for 6 days, followed by washing and drying. This resulted in the formation of a black powder with a high yield (83%). Both inductively coupled plasma optical emission spectroscopy (ICP-OES) and X-ray fluorescence spectroscopy (XRF) show a Ni:S ratio of around 0.25, consistent with the expected ratio for a framework with a formula of $\mathbf{Ni_3(THT)_2}$ (Table S1, Figure S1). Moreover, the Fe:Ni ratios are <0.06 across all batches, indicative of complete transmetalation under the experimental conditions. FT-IR data and a ^1H NMR spectrum after digestion rule out the presence of organic counterions, such as $Me_2NH_2^+$, which might affect the proposed formal oxidation state of the material (Figures S2 and S3). Powder X-ray diffraction (PXRD) analysis displays peaks almost identical to those of $\mathbf{Fe_3(THT)_2}$, suggesting preserved material crystallinity and morphology after transmetalation (Figures 2A, S4–S5). Further, Rietveld analysis using the reported structural model for $\mathbf{Fe_3(THT)_2}$ with Ni replacing Fe results in a good fit with negligible lattice parameter changes from $\mathbf{Fe_3(THT)_2}$ ($a = b =$ 22.703(8) Å and $c =$ 3.441(1) Å, Figures 2B and S6). We note that closely related materials to $\mathbf{Ni_3(THT)_2}$ have been previously reported and used in applications including electrocatalysis and electrochemical capture and release.[15,23,24] However, most of these materials are made in aqueous and/or aerobic conditions, and there is XPS evidence for O-

https://doi.org/10.1021/jacs.4c01860
J. Am. Chem. Soc. 2024, 146, 12063–12073

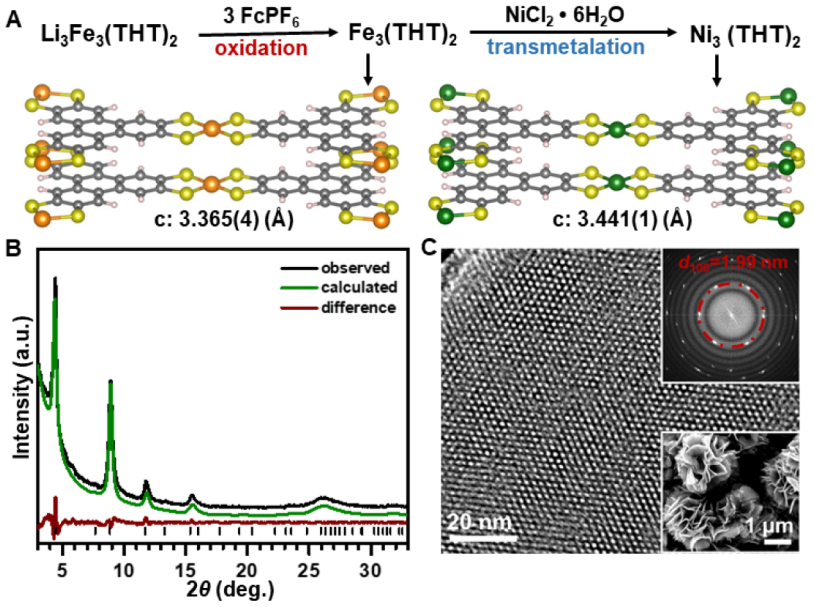

Figure 2. (A) Synthetic scheme for $Fe_3(THT)_2$ and $Ni_3(THT)_2$ through postsynthetic oxidation and transmetalation. Structural models of $Fe_3(THT)_2$ and $Ni_3(THT)_2$ showed similar interlayer distances through Rietveld analysis. Color code: orange, Fe; green, Ni; yellow, S; gray, C; pink, H. (B) Comparison of the experimental X-ray powder diffraction data and calculated pattern. (C) High-resolution TEM image of the 2D hexagonal structure of $Ni_3(THT)_2$; inset: the fast Fourier transform (top) and SEM image (bottom) showing the flake-like morphology.

incorporation in some cases. Even without this, the component redox states have not been thoroughly characterized, and detailed charge transport and/or electronic structure studies have not been reported. Thus, the aliovalent synthesis of $Ni_3(THT)_2$ provides a rigorously air- and water-free route to high purity and crystallinity material.

A preserved particle morphology is confirmed by scanning electron microscopy (SEM) images of $Ni_3(THT)_2$, which show a sheet-like morphology similar to $Fe_3(THT)_2$ and other related 2D stacked frameworks (Figure 2C bottom inset). High-resolution transmission electron microscopy (HRTEM) images reveal a hexagonal structure with crystalline domains of ~100's of nms, and a fast Fourier transform (FFT) further confirms a hexagonal lattice with a d(100) spacing of 1.99 nm (Figures 2C and S7). N_2 uptake experiments suggest a type I adsorption isotherm (microporous) and the measured Brunauer–Emmett–Teller (BET) surface area is 363.6 m^2/g (Figure S8). All of these data confirm that morphology, crystallinity, and porosity are preserved after metal substitution. As a synthetic note, attempts to directly synthesize $Ni_3(THT)_2$ by reacting the stannylated precursor **SnTHT** with Ni salts are not successful. Thus, this transmetalation strategy provides a unique synthetic access to this Ni-based material.

The formula of $Ni_3(THT)_2$ suggests either a Ni(III) redox state, presumably arising from in situ oxidation by Fe(III), or that the THT linker has been further oxidized to an overall −3 state if the Ni(II) oxidation state is preserved upon transmetalation. We therefore carried out X-ray photoelectron spectroscopy (XPS) to investigate the redox states of both Ni and the THT linkers in $Ni_3(THT)_2$. The high-resolution Ni 2p spectrum shows single symmetric Ni $2p_{3/2}$ (~854.6 eV) and Ni $2p_{1/2}$ (~871.9 eV) peaks, indicating the presence of Ni(II) (Figure 3 top).[25,26] In comparison, the high-resolution S 2p spectrum shows multiple overlapping signals between 162 and 166 eV, and displays a noticeable overall shift toward higher energy compared to $Fe_3(THT)_2$ (Figure 3 bottom). Peak deconvolution analysis shows the emergence of a higher energy

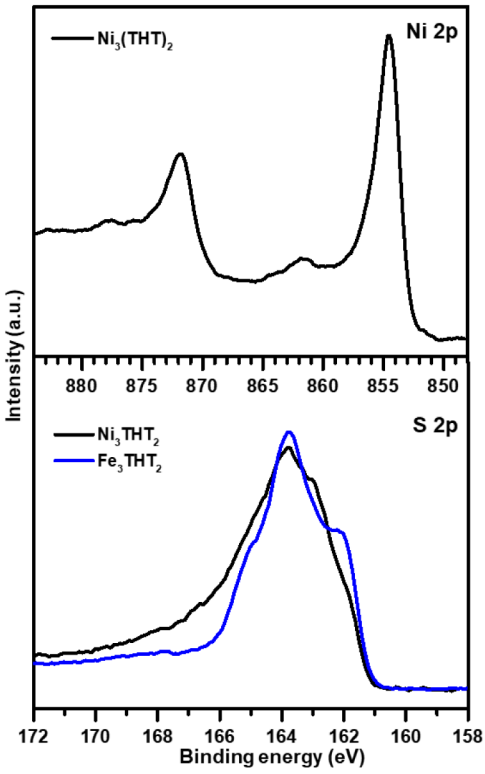

Figure 3. High-resolution Ni 2p spectrum (top) and comparison of S 2p XPS results for $Ni_3(THT)_2$ and $Fe_3(THT)_2$ (bottom).

feature (a doublet at ~165.9/167.1 eV) in $Ni_3(THT)_2$ (Figure S10). This observation suggests that the linker is further oxidized after replacing Fe(III) with Ni(II). This hypothesis is further supported by Raman spectroscopy. A peak at around 1550 cm^{-1}, which can be assigned to aromatic ring vibrations, shows a clear 11 cm^{-1} shift toward lower energy in $Ni_3(THT)_2$ than in $Fe_3(THT)_2$, consistent with triphenylene backbone

https://doi.org/10.1021/jacs.4c01860
J. Am. Chem. Soc. 2024, 146, 12063−12073

bond weakening upon further oxidation (Figure S11).[18,27] All of these data support the idea that Ni(II) substitutes into the $M_3(THT)_2$ lattice with a concurrent oxidation of the THT linker and formal displacement of Fe(III). These results are consistent with observations in molecular metal bis(dithiolene) systems where Ni usually prefers a +2 formal oxidation state.[28,29] While postsynthetic metal exchange or metal substitution in MOFs is an established technique to obtain new materials and modulate properties, these are usually isovalent substitutions, i.e., exchanging two divalent metals.[30,31] One key example is from Chen et al., who reported a continuous tuning of band gap and electrical conductivity in a 2D c-MOF system through isovalent alloying with Ni, Co, and Cu.[22] In contrast, the generation of $\mathbf{Ni_3(THT)_2}$ presented here is an unusual example in which a linker redox-state change is triggered by aliovalent metal substitution. We therefore worked to understand what effect these more oxidized THT linkers would have on the electronic structure and charge transport properties of this material.

Bulk Electronic Structure. $\mathbf{Ni_3(THT)_2}$ displays a broad intense absorption from 550 to 1100 nm by UV−vis−NIR diffuse reflectance spectroscopy (Figure S12a). Fourier-transform infrared (FT−IR) spectroscopy also exhibits this absorption with a rising edge at ∼2000 cm^{-1} (Figure S12b). A direct band gap Tauc analysis gives an absorption edge value of 0.40 eV that is similar to that observed in $\mathbf{Fe_3(THT)_2}$ (Figure 4A). The small optical band gap for the NIR absorption can be reasonably ascribed to the covalent Ni bis(dithiolene) units, extended conjugation in the 2D sheets, out-of-plane $\pi-\pi$ stacking interactions, and/or the mixed-valency of the redox-active dithiolene units.

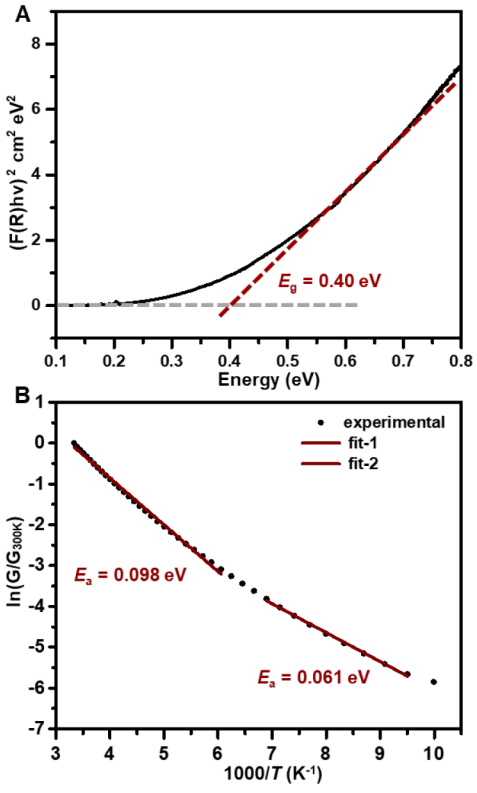

Figure 4. (A) Tauc plot with a direct band gap fitting (dashed line) for the near-IR edge. (B) Arrhenius fitting (solid line) of the variable-temperature conductance (G) data (black dots) at different temperature ranges.

The bulk electrical conductivity (σ) of $\mathbf{Ni_3(THT)_2}$ was measured using a four-probe method on pressed pellets to give an average value of 0.32(9) S cm^{-1} (Figure S13, Table S4). This value is ∼4× higher than the value of $\mathbf{Fe_3(THT)_2}$ ($7.8(3) \times 10^{-2}$ S cm^{-1}). The Seebeck coefficient (S) is −22.1 μV K^{-1} at room temperature, suggesting n-type thermoelectric behavior, which is also consistent with $\mathbf{Fe_3(THT)_2}$ (S = −20.7 μV K^{-1}).Variable-temperature resistance measurements from 100 to 300 K exhibit increasing resistance upon cooling, indicative of semiconducting behavior in $\mathbf{Ni_3(THT)_2}$ (Figure S14a). Interestingly, the plot of conductance in Figure 4B shows a distinctly nonlinear temperature dependence. Fitting the high and low temperature regions of these data with a nearest-neighbor hopping (NNH) model indicates small activation energies (E_a) of 0.098 eV above 160 K and 0.061 eV below 140 K.[32] These values are slightly higher than the corresponding values in $\mathbf{Fe_3(THT)_2}$. A better linear fit over the whole temperature range can be obtained with a Mott variable-range hopping model (Figure S14b). The fitted T_0 value is higher than that observed in $\mathbf{Fe_3(THT)_2}$, indicating a lower density of states around the Fermi level and consistent with the slightly higher hopping energy barrier.[32] It is known that the activation energy of hopping charge transport can be affected by magnetic interactions. For instance, the antiferromagnet $CaMnO_{3-\delta}$ shows an increasing activation energy with a decrease in temperature.[33,34] As $\mathbf{Fe_3(THT)_2}$ shows predominantly antiferromagnetic interactions, we also examined the magnetic interactions in $\mathbf{Ni_3(THT)_2}$.

The magnetic properties of $\mathbf{Ni_3(THT)_2}$ were investigated with variable temperature susceptibility measurements and the experimental $\chi_M T$ values display a generally decreasing trend with temperature indicating antiferromagnetic interactions (Figure S15a,b). Fitting the χ_M^{-1} data with the Curie−Weiss law below 200 K shows a Weiss constant (θ_{cW}) of −8.9 K that is smaller than that observed in $\mathbf{Fe_3(THT)_2}$ (−123.7 K), supporting weak antiferromagnetic exchange in this temperature region (Figure S15c). Variable-temperature zero-field-cooled and field-cooled DC magnetization data show no divergence (Figure S16). This suggests either the absence of any long-range antiferromagnetic ordering or potentially a geometrically frustrated spin system as discussed in a previously reported 2D semiconductive MOF.[35] We also note some curvature in the $\chi_M T$ values at higher temperatures. This might suggest some additional stronger antiferromagnetic interaction or perhaps a spin-transition in the material, but elucidating these trends will require additional high temperature measurements. It is worth noting that the magnetic interactions in $\mathbf{Fe_3(THT)_2}$ are complicated due to possible competing coupling between the M-M, M-L, and L-L pathways. We have tentatively proposed that the strong antiferromagnetic interaction starting at room temperature arises from metal−metal coupling along the 1D FeS_4 stacks, while the spins from the oxidized linkers may further weaken these interactions in a competing manner. In contrast, $\mathbf{Ni_3(THT)_2}$ putatively has a diamagnetic Ni(II) centers. The observed magnetic behavior below 200 K therefore corresponds to spins on the oxidized linkers which we propose couple more weakly.

We also performed Hall effect measurements to investigate the cause of the increased electrical conductivity in $\mathbf{Ni_3(THT)_2}$. These experiments were performed on pressed

https://doi.org/10.1021/jacs.4c01860
J. Am. Chem. Soc. 2024, 146, 12063−12073

pellets using the same method as in our previous report (Figure S17).[18] Interestingly, the measured Hall carrier concentration (N) at room temperature decreases 60-fold to $6.43(4) \times 10^{18}$ cm^{-3} from $\mathbf{Fe_3(THT)_2}$ ($3.97(7) \times 10^{20}$ cm^{-3}). Concurrently, the calculated Hall mobility (μ) increases 50-fold to 0.37 cm^2 V^{-1} s^{-1} compared to the value in $\mathbf{Fe_3(THT)_2}$ (1.69×10^{-3} cm^2 V^{-1} s^{-1}, Figure S18). These results suggest that the source of the increased conductivity in $\mathbf{Ni_3(THT)_2}$ is increased carrier mobility. This stands in contrast to $\mathbf{Fe_3(THT)_2}$ where a trend of increasing conductivity was observed as the carrier concentration increased upon stoichiometric oxidation. We hypothesize that replacing Fe^{3+} (d^5, $S = 3/2$) with Ni^{2+} (d^8, $S = 0$) in a square planar (D_{4h} symmetry) geometry decreases the carrier concentration in the $\mathbf{Ni_3(THT)_2}$ material.[15,17] In parallel, further oxidation of the dithiolene motifs may increase the dithioketone character in the THT linkers instead of resonance structures with formal ligand π radicals. This may further decrease the carrier concentration.[27,36] However, we rationalize that this higher degree of dithiolene oxidation also improves the covalency in $\mathbf{Ni_3(THT)_2}$ which leads to enhanced mobility and conductivity. Similar trends have been both experimentally and theoretically observed in bis(dithiolato) transition-metal complexes.[37,38] We therefore ascribe the increased Hall mobility in $\mathbf{Ni_3(THT)_2}$ to the improved covalency.

As a final investigation of transport properties, variable-temperature Hall effect measurements were also performed from 120 to 300 K. A decreasing trend in carrier concentration with decreasing temperature is observed, consistent with semiconducting behavior (Table S5, Figure S19a). The calculated activation energy of 0.129 eV is also slightly higher than that observed in $\mathbf{Fe_3(THT)_2}$ by using the same method (Figure S19b). All these data are consistent with the variable-temperature conductivity measurements and further confirm that these THT materials are small bandgap semiconductors with hopping as the major charge transport mechanism.

Computational Modeling. To further explain the behavior and electronic properties of $\mathbf{Ni_3(THT)_2}$, we turned to computational modeling. We based our calculations on periodic density functional theory (PBC-DFT) to describe the molecular and electronic structure of $\mathbf{Ni_3(THT)_2}$. All calculations were performed with the hybrid functional HSE06-D3BJ[39,40] in the gas phase for both the structure optimization and the band structure. HSE06 provides more reliable results compared to the widely used PBE+U, which is highly dependent on the parametrization of U (Tables S5 and S6)).[41,42] Our calculations started from various broken symmetry guesses (see SI) that describe different electronic structures considering formally trianionic THT ligands together with high and low spin states associated with the Ni(II) centers, with an overall disposition of three unpaired electrons per ligand and up to two unpaired electrons per Ni center (Table S4). The location of different spin state solutions is fundamental to explain the observed magnetic behavior.

From nine starting guesses (Table S6), we obtained two major electronic state solutions: the ground state antiferromagnetic open-shell singlet (**BS2h**), and a ladder of many higher energy states with increasing ferromagnetic character (**BS6h**). The ground state **BS2h** is a singlet state showing zero spin density on Ni and a small amount of antiferromagnetic spin density on the THT ligands (Figure 5, top, note the small isovalue to make the surface more visible). From the ground state, the next nearest solutions **BS6h** and **BS6h'** are 0.8 and

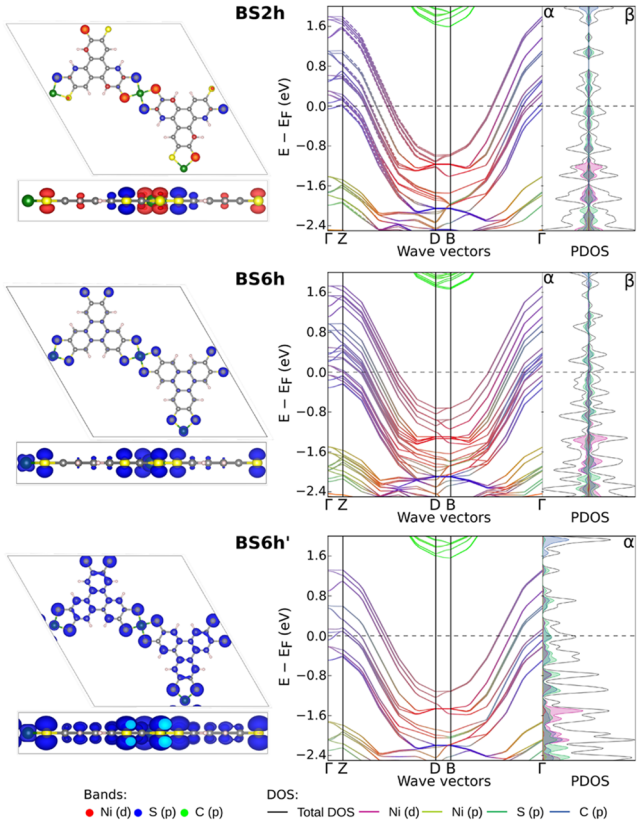

Figure 5. Spin density, band structure, and projected density of state (PDOS) of $\mathbf{Ni_3(THT)_2}$ in the ground state singlet **BS2h** (top, E_F = −1.19 eV) and ferromagnetic **BS6h** (middle, E_F = −1.28 eV), and **BS6h'** (bottom, E_F = −1.19 eV) solutions calculated with the HSE06 functional. Isovalue of 0.001 e/Å^3, PDOS Gaussian broadening of 0.04. Ni shown in green, S in yellow, C in gray, H in pink, spin up in blue, spin down in red.

2.8 kcal/mol higher in electronic energy, respectively. These two solutions show increasing ferromagnetic character on both Ni centers and ligands. The spin density on the Ni center is about 0.06 and 0.07, and on the ligands 0.2 and 0.6, respectively, for **BS6h**, and **BS6h'** (Figure 5 and SI). The trend of increasing ferromagnetic character continues to even higher energy solutions, such as **BS6h''** and **BS6h'''**, which are located at 9.9 and 22.9 kcal/mol in electronic energy, respectively, from the ground state **BS2h**. The spin density on the Ni center is about 0.13 and 0.27, and on the ligands 1.2 and 1.7, respectively, for **BS6h''**, and **BS6h'''** (Table S7). These latter two solutions are too high in energy to be thermally accessible at the temperature range of this study. The increased spin density builds up primarily on the S of the THT ligands. These results suggest noninnocent ligand behavior with some electron density partially moving between the THT ligand and the Ni centers (Figure 5 and SI). The increased spin density on the ligands, together with the transition from a singlet state toward a doublet-like state on the Ni centers, could be related to partial transition from Ni(II) centers toward Ni(III) centers; in fractional units, the oxidation state could be considered as ∼2.2. Most importantly, the relative energetic separations of about 1 and 3 kcal/mol from the ground state of the lower ferromagnetic states (**BS6h** and **BS6h'**), and the higher number of unpaired e^- may explain the increase in magnetic susceptibility in $\mathbf{Ni_3(THT)_2}$ with the rise of the temperature.

https://doi.org/10.1021/jacs.4c01860
J. Am. Chem. Soc. 2024, 146, 12063−12073

Band structure calculations clearly show the absence of a visible band gap (Figure 5, top right and S20). The first conduction band primarily involves ligand S atoms (blue color) in the ground state **BS2h**. This is consistent with diamagnetic Ni(II) centers with most of the carriers localized on the THT linkers. In contrast, the conduction band shows slightly more Ni-character (red color) in **BS6h** and **BS6h'** (Figures 5 middle, bottom and S21). These two solutions may offer some explanation for the change in charge transport properties upon temperature variation.

$Ni_3(THT)_2$ has been synthesized via transmetalation from a previously published MOF, $Fe_3(THT)_2$,[18] by swapping Fe for Ni. While these systems are clearly related, they show very different electronic structures and spin densities. For a more authentic comparison, the electronic structure of $Fe_3(THT)_2$ was also calculated at the same level of theory as that for $Ni_3(THT)_2$ described above. The computational results show that the spin density in $Fe_3(THT)_2$ is mostly located at the Fe centers. Furthermore, no ladder of broken symmetry structures was found in $Fe_3(THT)_2$. Instead, two almost degenerate electronic structures were found (**BS7h** and **BS8h**, Figure 6).

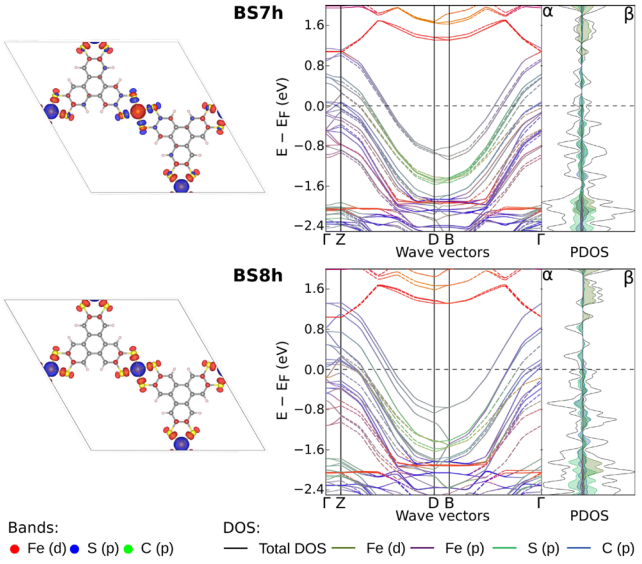

Figure 6. Spin density, band structure, and projected density of state (PDOS) of $Fe_3(THT)_2$ in the ground state singlet **BS7h** (top, E_F = −1.76 eV) and ferromagnetic **BS8h** (bottom, E_F = −1.77 eV) solutions calculated with the HSE06 functional. Isovalue of 0.003 *e*/Å^3, PDOS Gaussian broadening of 0.04. Fe shown in orange, S in yellow, C in gray, H in pink, spin up in blue, spin down in red.

This is in contrast to $Ni_3(THT)_2$ where the spin density is mainly localized on the ligand. The most stable calculated electronic structures, antiferromagnetic **BS7h** and ferromagnetic **BS8h**, have the same spin density values but different phases on the Fe centers. We note that both the **BS7h** and **BS8h** solutions were converged starting from many of the same initial guesses used for $Ni_3(THT)_2$ and no other local minima close in energy could be located. The oxidation state of the Fe centers is between II and III and the spin multiplicity is closest to a quartet state (2.6 unpaired e^- per Fe) with little spin density on the ligands. The THT ligands also have a comparatively more negative charge in $Fe_3(THT)_2$ than in $Ni_3(THT)_2$, consistent with the experimentally observed ligand oxidation. The electronic energy difference between the antiferromagnetic **BS7h** and ferromagnetic **BS8h** states is 0.35 kcal/mol. To compare these values with $Ni_3(THT)_2$, we can consider the energy of the state with the most similar ligand-based spin density to **BS8h, BS6h'** (Tables S7 and S9). The energy difference between **BS2h** and **BS6h'** is 2.82 kcal/mol, which is significantly larger than the energetic difference between **BS7h** and **BS8h**. We tentatively propose that this larger energetic splitting in $Ni_3(THT)_2$ may be a possible explanation for the distinct charge transport regions as well as the increasing moment at temperatures >200 K.

Electrochemical Properties. 2D c-MOFs with high electrical conductivity and intrinsic porosity can allow fast transport of electrons and ions, making them promising platforms for electrochemical energy storage. Many reports have shown good performance of these materials as batteries and supercapacitors.[5,43−47] We were therefore interested in investigating how the variable metal and linker oxidation states in these THT-based materials would influence their electrochemical properties, and thus, we conducted cyclic voltammetry (CV) experiments in a three-electrode system. We coated both $Ni_3(THT)_2$ and $Fe_3(THT)_2$ onto conductive paper as a working electrode, a platinum flag was used as a counter electrode, and Ag wire was used as a pseudoreference electrode (see experimental details). CV data collected in 0.2 M $LiPF_6$/DMF electrolyte reveal markedly different electrochemical behavior for $Fe_3(THT)_2$ and $Ni_3(THT)_2$. Specifically, irreversible or quasi-reversible peaks are observed for $Fe_3(THT)_2$ over a potential range of −0.8 to 0.8 V (vs ferrocene/ferrocenium, Fc/Fc^+) and no obvious Faradaic peak or capacitive behavior is observed between 0.9 V and −2.6 V (Figure S24). Electrochemical decomposition of this coated material can be seen after one cycle and is especially clear when it is cycled anodically above −0.5 V.

In comparison, $Ni_3(THT)_2$ displays an improved electrochemical stability without any decomposition during cycling. The CV of $Ni_3(THT)_2$ shows irreversible peaks above −0.5 V but a broad symmetric waveform between −0.7 and −1.4 V (vs Fc/Fc^+) (Figure 7A). Further scans suggest this profile is preserved under different scan rates, albeit with some distortion at high scan rates (Figures 7B and S25). This feature indicates a dominant pseudocapacitive charge storage mechanism in this material.[47,48] To investigate this charge storage mechanism, CV curves of $Ni_3(THT)_2$ electrodes were further collected at scan rates ranging from 1 to 15 mV s^{-1} in a $LiPF_6$/DMF or $LiPF_6$/MeCN electrolyte (Figures 7B and S26b). We initially used a basic assay (referred to as b-value analysis) to determine whether this feature arose from a diffusion-controlled battery-type process or a surface-controlled capacitive (or pseudocapacitive) process.[47−49] In the former process, the peak current scales with the square root of the sweep rate. In contrast, surface-controlled processes have a peak current that scales linearly with the sweep rate. Plotting the log of peak current density vs the log of the scan rate shows a linear relationship with slope b-values close to 1 indicative of dominant surface-controlled redox capacitance (shown in Figures 7C and S26c). Specific capacitances calculated from these curves are 67 F/g in $LiPF_6$/DMF and 47 F/g in $LiPF_6$/MeCN at a scan rate of 1 mV s^{-1} (Figures 7D and S26d). The slightly lower specific capacitance and cathodically shifted peak window in MeCN may be ascribed to the slower ion adsorption and desorption during the surface-confined redox process. Although these values are relatively low compared to other 2D c-MOFs,[43,47] the much better performance and

https://doi.org/10.1021/jacs.4c01860
J. Am. Chem. Soc. 2024, 146, 12063−12073

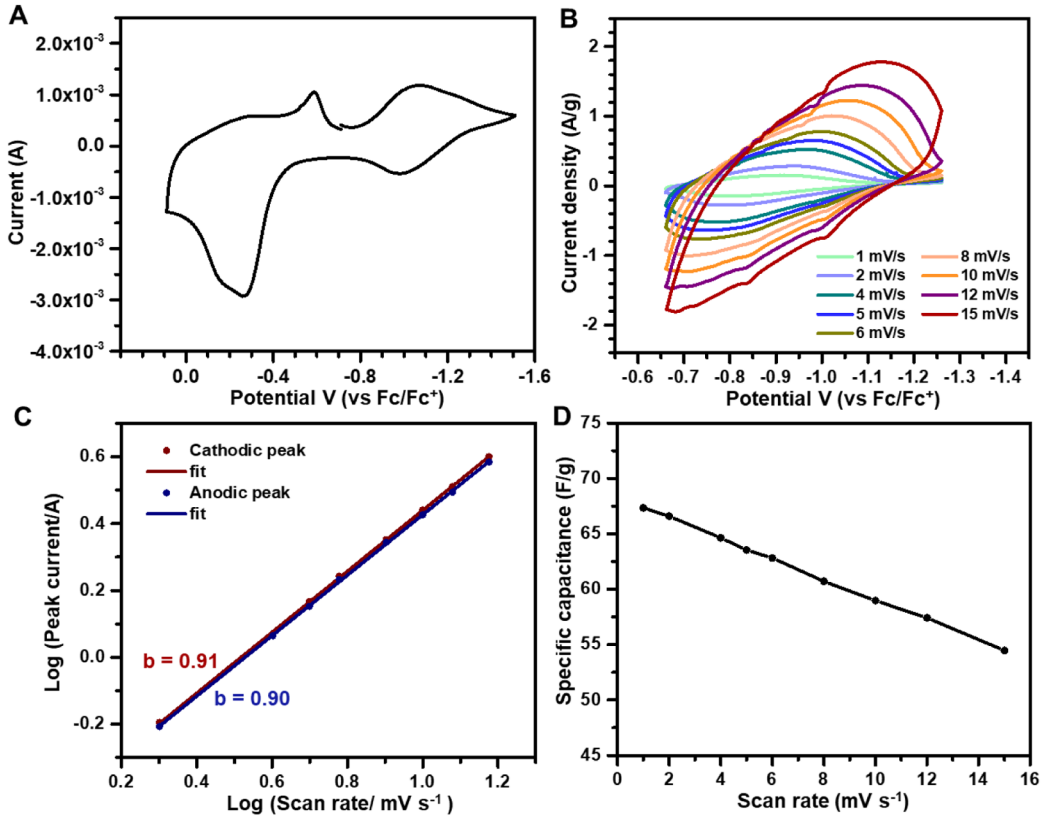

Figure 7. (A) CV of $Ni_3(THT)_2$ in a 0.2 M $LiPF_6$/DMF electrolyte with a scan rate of 10 mV s^{-1}. (B) CV of $Ni_3(THT)_2$ in 0.2 M $LiPF_6$/DMF electrolyte with various scan rates. (C) Log peak current versus log scan rate plots (dots) and corresponding linear fit (solid line). (D) Specific capacitances calculated from CV curves as a function of scan rates.

stability of $Ni_3(THT)_2$ versus $Fe_3(THT)_2$ illustrates how aliovalent substitution can facilitate improved or altered electrochemical behavior as well.

CONCLUSIONS

In this work, we have demonstrated access to a 2D c-MOF, $Ni_3(THT)_2$, through a novel aliovalent substitution. Transmetalation of Fe(III) to Ni(II) results in in situ linker oxidation, which modulates material electronic properties. It results in higher electrical conductivity and Hall mobility but slightly lower carrier densities and weaker antiferromagnetic interactions in the Ni material. Furthermore, Ni for Fe substitution leads to improved material electrochemical stability and thus enables pseudocapacitive behavior. Initial analyses indicated surface-controlled capacitive charge storage in $Ni_3(THT)_2$. These results emphasize how aliovalent substitution of 2D c-MOFs can tune their electronic structure. This strategy, while well-established in other solid-state materials, is comparatively underexplored in MOFs. Our results here motivate the expanded use of aliovalent substitution to tune the redox-states and properties of c-MOFs more broadly.

EXPERIMENTAL SECTION

General Considerations. All material syntheses and characterizations were performed in a N_2-filled glovebox or under N_2 protection. Dimethylformamide (DMF) and acetonitrile (MeCN) were initially dried on a solvent purification system from Pure Process Technology and were further treated by passing through activated alumina and stored over 4 Å molecular sieves in the glovebox. All other chemicals were purchased from commercial sources and used as received.

Synthesis of $Ni_3(THT)_2$. Freshly made $Fe_3(THT)_2$ (120 mg) was soaked in 0.2 M $NiCl_2 \bullet 6H_2O$ solutions (3 × 15 mL, DMF) at 70 °C for 6 days, decanting the mother liquor and adding fresh solution every other day. After three soaks, the remaining solid was washed thoroughly with fresh DMF (3 × 15 mL) and CH_3CN (3 × 15 mL) by soaking the solid in the fresh solvent for a few hours followed by decanting. The resulting black powder was dried under vacuum overnight at room temperature (100 mg, 83%).

X-Ray Powder Diffraction (PXRD). Laboratory PXRD data were acquired on a Rigaku MiniFlex benchtop X-ray diffractometer equipped with Cu Kα radiation in a Bragg−Brentano reflection geometry. The data analysis was carried out by using GSAS-II software.

Scanning Electron Microscopy (SEM). SEM images were taken on a Carl Zeiss Merlin electron microscope using the In-Lens detector at the Materials Research Science and Engineering Center (MRSEC) at the University of Chicago. The sample powder was dispersed on conductive tape substrates, and an accelerating voltage of 5.00 kV was applied for the measurement.

Transmission Electron Microscopy (TEM). TEM images were taken on an FEI Tecnai F30 electron microscope. The sample powder was dispersed in MeCN and sonicated for about five min before loading onto the copper grid. High-resolution transmission electron microscopy (HRTEM) images were processed with ImageJ software.

Nitrogen Adsorption Measurement. Sample powder was loaded in an analysis tube in the glovebox and capped with a Transeal. The sample tube was degassed at 80 °C for 3 days until an outgas rate of less than 1 mTorr/min was observed. The N_2 adsorption isotherm at 77 K was measured in liquid nitrogen. After the experiment, the PXRD pattern of the sample was checked and the crystallinity was maintained.

https://doi.org/10.1021/jacs.4c01860
J. Am. Chem. Soc. 2024, 146, 12063−12073

Digestion and ICP-OES Measurements. ICP-OES analysis was carried out using an Agilent 700 series spectrometer. Digestion procedures were adapted from literature reports.[50] Around 2 mg of each material was digested in 1.0 mL of HNO_3 and 1.0 mL of H_2O_2 (both trace metal grade) in tightly sealed high-density polyethylene (HDPE) centrifuge tubes overnight. The solution was further diluted to the 1−25 ppm range with ultrafiltered deionized water. The absolute element concentration (Table S1) was obtained from a freshly made external calibration curve. The averaged element concentration from two characteristic emission wavelengths for each element was used to calculate the final Ni/S and Fe/Ni ratio.

X-Ray Fluorescence Spectroscopy (XRF). The sample powder was ground with a mortar and pestle and was prepared as a pressed pellet (7 mm diameter). The data were collected on a Rigaku NEX DE VS spectrometer under a He atmosphere. The results were externally calibrated to a commercial multielement standard.

X-Ray Photoelectron Spectroscopy (XPS). XPS spectra were collected on an AXIS Nova spectrometer (Kratos Analytical) equipped with a monochromatic Al Kα X-ray source. The instrument work function was calibrated to give a Au 4f7/2 metallic gold binding energy of 83.95 eV. For calibration purposes, the binding energies were referenced to the C 1s peak at 284.8 eV. Survey spectra were collected with a step size of 1 and 160 eV pass energy. The high-resolution spectra were collected with a pass energy of 40 and 0.1 eV step size.

UV−Vis−NIR Spectroscopy. Solid UV−vis−NIR diffuse reflectance spectra were collected on a Thermo Scientific Evolution 300 spectrometer with powder samples loaded in a Praying Mantis air-free diffuse reflectance cell using KBr powder as the nonadsorbing matrix. The Kubelka−Munk conversion of the raw diffuse reflectance spectrum was obtained by applying the formula $F(R) = (1-R)^2/2R$.

FT−IR Spectroscopy. Powder samples for FT-IR spectroscopy were pressed into pellets in a potassium bromide matrix. Spectra were acquired in transmission mode on a Bruker Tensor II spectrometer with MCT detector operated at 77 K. Data were processed with background subtractions.

Raman Spectroscopy. Powder samples were pressed into pellets and sealed between two glass slides by using an imaging spacer in the glovebox. Raman spectra were obtained with a Horiba LabRamHR Evolution confocal microscope. A Si (111) wafer was used for calibration. The sample was excited using a 473 nm light source operating at 2−10% of its maximum power and using 100× long path objective and a 600 mm^{-1} grating.

Four-Probe Conductivity and Seebeck Coefficient Measurements. Room temperature four-probe conductivity and Seebeck coefficient measurements were performed using a custom designed probe station in an argon glovebox with a well-established method.[51] Around 20 mg of the sample powder was pressed into a pellet with a diameter of 8 mm. Gold electrical contacts (~100 nm thick) were deposited onto the pressed pellet (200−400 μm thick) via thermal evaporation in a glovebox (Figure S13a). The Seebeck coefficient was calculated from the slope of a linear fit for the ΔV vs ΔT plot. For each sample, both a forward and a reverse scan were carried out to obtain an average Seebeck value and a coefficient of 1.2 was divided to adjust the geometry.[52] The resistance (R, ohm) of the sample pellet was extracted from the slope of the $I-V$ sweep. The conductivity σ was then calculated via the following equation after geometry correction:[53]

$$\sigma = \frac{\ln\left(\frac{\sinh\frac{t}{S}}{\sinh\frac{t}{2S}}\right)}{\pi R t}$$

where R is the measured resistance, t is the thickness of the sample, and S is the probe spacing (200 μm).

Variable Temperature Conductivity and Hall Effect Measurements. The VT-conductivity and Hall effect measurements were carried out on a Quantum Design Physical Property Measurement System (PPMS) using the Model 6000 controller. Specific gold electrical contacts (~100 nm thick) were deposited onto the pressed sample pellets (6 mm × 3 mm) to form a Hall bar in an argon filled glovebox. The sample pellet was further mounted to a DC Resistivity/ETO Sample Puck (P102) through indium-wire bonding in a N_2-filled glovebox (Figures S14 and S17). Detailed procedures and calculations have been previously reported.[18]

Magnetic Measurements. Magnetic measurements were performed on a Quantum Design MPMS3 SQUID magnetometer. Bulk powder (~10 mg) was carefully massed and then suspended in an eicosane matrix in a polycarbonate capsule to prevent movement and protect the sample from incident air exposure in a N_2-filled glovebox. Diamagnetic corrections for the capsule and eicosane were made by measuring temperature vs moment in triplicate for each sample to determine a moment per gram correction. Diamagnetic corrections for the sample itself were applied using Pascal's constants of each atom based on the formula of $\mathbf{Ni_3(THT)_2}$.[54]

Electrode Fabrication and Electrochemical Measurements. $\mathbf{Ni_3(THT)_2}$, Super P carbon black, and poly(vinylidene fluoride) with a mass ratio of 80:10:10 were mixed in *N*-methyl-2-pyrrolidone as a slurry in the glovebox. The electrode slurry was drop-cast on the bottom half surface of a 2.5 cm × 1 cm conductive carbon paper (Thermo scientific, Toray carbon paper, cleaned by plasma before use) and dried under vacuum at 50 °C. The mass of each substrate was measured before and after coating to determine the mass of active material deposited (~1−2 mg per sample). The CV experiments were performed using a BASi Epsilon potentiostation/Galvano station fitted to a N_2 glovebox. During tests, the carbon paper electrode was connected to a Pt clamp and used as the working electrode; a platinum flag was used as a counter electrode and an Ag wire was used as pseudoreference electrode. The potential was referenced to ferrocene/ferrocenium (Fc/Fc+) by scanning the CV of ferrocene using a blank carbon paper electrode ($E_{1/2}$ = 0.71 V). The specific capacitance (F/g) was calculated from cyclic voltammetry by the following formula:

$$C = \int IdV/[2mv(V_f - V_i)]$$

where $\int IdV$ implies the area under the CV curve; m signifies the material mass, v refers to the scan rate, and $(V_f - V_i)$ is the potential window.

Computational Methods. Periodic density functional theory (PBC-DFT) calculations were performed on a single unit cell of each considered species using the Vienna Ab Initio Simulation Package (VASP 6.4.0).[55,56] Both the Heyd−Scuseria−Ernzerhof HSE06,[39] and Perdew−Burke−Ernzerhof PBE exchange-correlation density functional[33] were used along with Grimme's D3 dispersion correction with Becke−Johnson damping (D3BJ)[40] were used for geometry optimization and band structure calculation. A plane-wave basis set with a kinetic energy cutoff of 520 eV was used for the geometry optimizations, and a normal pseudopotential was used for all atoms.[57] When the PBE functional was used, the Coulomb and exchange interactions of the localized d-orbitals in Ni centers were treated within the framework using the DFT + U method.[42] The effective Coulomb (U) and exchange (J) parameters were set at U = 4 eV and J = 0 eV.[18] Energy and force convergence criteria of 10^{-6} eV and 0.01 eV $Å^{-1}$, respectively, were employed for all optimizations. A 1 × 1 × 7 and a 3 × 3 × 23 Γ-centered k-point grid was used for the Brillouin zone sampling for the structure optimization with functionals HSE06-D3BJ and PBE-D3BJ, respectively. Density of state has been calculated at the same optimization level, increasing the mapping points with (NEDOS = 5000). Band structures at the HSE06 level were calculated using nonuniform explicit k-points.

■ ASSOCIATED CONTENT

Supporting Information

The Supporting Information is available free of charge at https://pubs.acs.org/doi/10.1021/jacs.4c01860.

Additional experimental details and characterization data (PDF)

https://doi.org/10.1021/jacs.4c01860
J. Am. Chem. Soc. 2024, 146, 12063−12073

AUTHOR INFORMATION

Corresponding Author

John S. Anderson − *Department of Chemistry, University of Chicago, Chicago, Illinois 60637, United States;* orcid.org/0000-0002-0730-3018; Email: jsanderson@uchicago.edu

Authors

Lei Wang − *Department of Chemistry, University of Chicago, Chicago, Illinois 60637, United States;* orcid.org/0000-0002-3778-2814

Andrea Daru − *Department of Chemistry, University of Chicago, Chicago, Illinois 60637, United States;* orcid.org/0000-0002-0825-2101

Bhavnesh Jangid − *Department of Chemistry, University of Chicago, Chicago, Illinois 60637, United States;* orcid.org/0000-0001-6048-4981

Jie-Hao Chen − *Pritzker School of Molecular Engineering, University of Chicago, Chicago, Illinois 60637, United States;* orcid.org/0009-0006-8843-0639

Ningxin Jiang − *Department of Chemistry, University of Chicago, Chicago, Illinois 60637, United States*

Shrayesh N. Patel − *Pritzker School of Molecular Engineering, University of Chicago, Chicago, Illinois 60637, United States;* orcid.org/0000-0003-3657-827X

Laura Gagliardi − *Department of Chemistry and Pritzker School of Molecular Engineering, University of Chicago, Chicago, Illinois 60637, United States; James Franck Institute, University of Chicago, Chicago, Illinois 60637, United States;* orcid.org/0000-0001-5227-1396

Complete contact information is available at: https://pubs.acs.org/10.1021/jacs.4c01860

Notes

The authors declare no competing financial interest.

ACKNOWLEDGMENTS

This research was supported by the U.S. National Science Foundation (DMR-2315924) and as part of the Catalyst Design for Decarbonization Center, an Energy Frontier Research Center funded by the U.S. Department of Energy, Office of Science, Basic Energy Sciences under award no. DE-SC0023383 particularly for the computational work. This work was partially supported by and used instrumentation from the University of Chicago Materials Research Science and Engineering Center, which is funded by the National Science Foundation under award number DMR-2011854. J.S.A. gratefully acknowledges the support from the Dreyfus Foundation for a teacher-scholar award (TC-21-064). We acknowledge the University of Chicago's Research Computing Center (RCC) for providing the resources to carry out the computational work.

REFERENCES

(1) Hmadeh, M.; Lu, Z.; Liu, Z.; Gándara, F.; Furukawa, H.; Wan, S.; Augustyn, V.; Chang, R.; Liao, L.; Zhou, F.; et al.et al. New Porous Crystals of Extended Metal-Catecholates. *Chem. Mater.* **2012**, *24* (18), 3511−3513.

(2) Sheberla, D.; Sun, L.; Blood-Forsythe, M. A.; Er, S.; Wade, C. R.; Brozek, C. K.; Aspuru-Guzik, A.; Dincă, M. High Electrical Conductivity in Ni_3(2,3,6,7,10,11-hexaiminotriphenylene)$_2$, a Semiconducting Metal−Organic Graphene Analogue. *J. Am. Chem. Soc.* **2014**, *136* (25), 8859−8862.

(3) Wang, M.; Dong, R.; Feng, X. Two-Dimensional Conjugated Metal−Organic Frameworks (2D c-MOFs): Chemistry and Function for MOFtronics. *Chem. Soc. Rev.* **2021**, *50* (4), 2764−2793.

(4) Sun, L.; Liao, B.; Sheberla, D.; Kraemer, D.; Zhou, J.; Stach, E. A.; Zakharov, D.; Stavila, V.; Talin, A. A.; Ge, Y.; Allendorf, M. D. A Microporous and Naturally Nanostructured Thermoelectric Metal-Organic framework with Ultralow Thermal Conductivity. *Joule* **2017**, *1* (1), 168−177.

(5) Feng, D.; Lei, T.; Lukatskaya, M. R.; Park, J.; Huang, Z.; Lee, M.; Shaw, L.; Chen, S.; Yakovenko, A. A.; Kulkarni, A.; et al.et al. Robust and Conductive Two-Dimensional Metal−Organic Frameworks with Exceptionally High Volumetric and Areal Capacitance. *Nat. Energy* **2018**, *3* (1), 30−36.

(6) Dong, R.; Zhang, Z.; Tranca, D. C.; Zhou, S.; Wang, M.; Adler, P.; Liao, Z.; Liu, F.; Sun, Y.; Shi, W.; Zhang, Z.; Zschech, E.; Mannsfeld, S. C. B.; Felser, C.; Feng, X. A Coronene-Based Semiconducting Two-Dimensional Metal-Organic Framework with Ferromagnetic Behavior. *Nat. Commun.* **2018**, *9* (1), 2637.

(7) Arora, H.; Dong, R.; Venanzi, T.; Zscharschuch, J.; Schneider, H.; Helm, M.; Feng, X.; Cánovas, E.; Erbe, A. Demonstration of a Broadband Photodetector Based on a Two-Dimensional Metal−Organic Framework. *Adv. Mater.* **2020**, *32* (9), 1907063.

(8) Liu, J.; Yang, D.; Zhou, Y.; Zhang, G.; Xing, G.; Liu, Y.; Ma, Y.; Terasaki, O.; Yang, S.; Chen, L. Tricycloquinazoline-Based 2D Conductive Metal−Organic Frameworks as Promising Electrocatalysts for CO_2 Reduction. *Angew. Chem., Int. Ed.* **2021**, *60* (26), 14473−14479.

(9) Xie, L. S.; Skorupskii, G.; Dincă, M. Electrically Conductive Metal−Organic Frameworks. *Chem. Rev.* **2020**, *120* (16), 8536−8580.

(10) Ko, M.; Mendecki, L.; Mirica, K. A. Conductive Two-Dimensional Metal−Organic Frameworks as Multifunctional Materials. *Chem. Commun.* **2018**, *54* (57), 7873−7891.

(11) D'Alessandro, D. M. Exploiting Redox Activity in Metal−Organic Frameworks: Concepts, Trends and Perspectives. *Chem. Commun.* **2016**, *52* (58), 8957−8971.

(12) Snook, K. M.; Zasada, L. B.; Chehada, D.; Xiao, D. J. Oxidative control over the Morphology of Cu_3(HHTP)$_2$, a 2D Conductive Metal−Organic Framework. *Chem. Sci.* **2022**, *13* (35), 10472−10478.

(13) Stodolka, M.; Choi, J. Y.; Flood, J.; Pham, H. T.; Park, J. Iron-Based 2D Conductive Metal−Organic Framework Nanostructure with Enhanced Pseudocapacitance. *ACS Appl. Nano Mater.* **2022**, *5* (2), 2156−2162.

(14) Contreras-Pereda, N.; Pané, S.; Puigmartí-Luis, J.; Ruiz-Molina, D. Conductive Properties of Triphenylene MOFs and COFs. *Coord. Chem. Rev.* **2022**, *460*, 214459.

(15) Kambe, T.; Sakamoto, R.; Kusamoto, T.; Pal, T.; Fukui, N.; Hoshiko, K.; Shimojima, T.; Wang, Z.; Hirahara, T.; Ishizaka, K.; et al.et al. Redox Control and High Conductivity of Nickel Bis(dithiolene) Complex π-Nanosheet: A Potential Organic Two-Dimensional Topological Insulator. *J. Am. Chem. Soc.* **2014**, *136* (41), 14357−14360.

(16) Clough, A. J.; Skelton, J. M.; Downes, C. A.; de la Rosa, A. A.; Yoo, J. W.; Walsh, A.; Melot, B. C.; Marinescu, S. C. Metallic Conductivity in a Two-Dimensional Cobalt Dithiolene Metal−Organic Framework. *J. Am. Chem. Soc.* **2017**, *139* (31), 10863−10867.

(17) Dong, R.; Han, P.; Arora, H.; Ballabio, M.; Karakus, M.; Zhang, Z.; Shekhar, C.; Adler, P.; Petkov, P. S.; Erbe, A.; et al.et al. High-Mobility Band-Like Charge Transport in A Semiconducting Two-Dimensional metal−organic framework. *Nat. Mater.* **2018**, *17* (11), 1027−1032.

(18) Wang, L.; Sarkar, A.; Grocke, G. L.; Laorenza, D. W.; Cheng, B.; Ritchhart, A.; Filatov, A. S.; Patel, S. N.; Gagliardi, L.; Anderson, J. S. Broad Electronic Modulation of Two-Dimensional Metal−Organic Frameworks over Four Distinct Redox States. *J. Am. Chem. Soc.* **2023**, *145* (15), 8486−8497.

(19) Woodward, P.; Karen, P.; Evans, J.; Vogt, T. *Solid State Materials Chemistry*; Cambridge University Press: Cambridge, 2021.

(20) You, F.; Liang, F.; Huang, Q.; Hu, Z.; Wu, Y.; Lin, Z. $Pb_2GaF_2(SeO_3)_2Cl$: Band Engineering Strategy by Aliovalent

Substitution for Enlarging Bandgap while Keeping Strong Second Harmonic Generation Response. *J. Am. Chem. Soc.* **2019**, *141* (2), 748−752.
(21) Chaudhary, M.; Karmakar, A.; Mishra, V.; Bhattacharya, A.; Mumbaraddi, D.; Mar, A.; Michaelis, V. K. Effect of Aliovalent Bismuth Substitution on Structure and Optical Properties of $CsSnBr_3$. *Commun. Chem.* **2023**, *6* (1), 75.
(22) Chen, T.; Dou, J.-H.; Yang, L.; Sun, C.; Libretto, N. J.; Skorupskii, G.; Miller, J. T.; Dincă, M. Continuous Electrical Conductivity Variation in M_3(Hexaiminotriphenylene)$_2$ (M = Co, Ni, Cu) MOF Alloys. *J. Am. Chem. Soc.* **2020**, *142* (28), 12367−12373.
(23) Dong, R.; Pfeffermann, M.; Liang, H.; Zheng, Z.; Zhu, X.; Zhang, J.; Feng, X. Large-AreaFree-Standing Two-Dimensional Supramolecular Polymer Single-Layer Sheets for Highly Efficient Electrocatalytic Hydrogen Evolution. *Angew. Chem., Int. Ed.* **2015**, *54* (41), 12058−12063.
(24) Mendecki, L.; Ko, M.; Zhang, X.; Meng, Z.; Mirica, K. A. Porous Scaffolds for Electrochemically Controlled Reversible Capture and Release of Ethylene. *J. Am. Chem. Soc.* **2017**, *139* (48), 17229−17232.
(25) Liu, Z.; Liu, T.; Savory, C. N.; Jurado, J. P.; Reparaz, J. S.; Li, J.; Pan, L.; Faul, C. F. J.; Parkin, I. P.; Sankar, G.; Matsuishi, S.; Campoy-Quiles, M.; Scanlon, D. O.; Zwijnenburg, M. A.; Fenwick, O.; Schroeder, B. C. Controlling the Thermoelectric Properties of Organometallic Coordination Polymers via Ligand Design. *Adv. Funct. Mater.* **2020**, *30* (32), 2003106.
(26) Xie, J.; Pan, J.-A.; Cheng, B.; Ma, T.; Filatov, A. S.; Patel, S. N.; Park, J.; Talapin, D. V.; Anderson, J. S. Presynthetic Redox Gated Metal-to-Insulator Transition and Photothermoelectric Properties in Nickel Tetrathiafulvalene-Tetrathiolate Coordination Polymers. *J. Am. Chem. Soc.* **2022**, *144* (41), 19026−19037.
(27) Sproules, S.; Wieghardt, K. o-Dithiolene and o-Aminothiolate Chemistry of Iron: Synthesis, Structure and Reactivity. *Coord. Chem. Rev.* **2010**, *254* (13), 1358−1382.
(28) Eisenberg, R.; Gray, H. B. Noninnocence in Metal Complexes: A Dithiolene Dawn. *Inorg. Chem.* **2011**, *50* (20), 9741−9751.
(29) Sproules, S.; Wieghardt, K. Dithiolene Radicals: Sulfur K-edge X-ray Absorption Spectroscopy and Harry's Intuition. *Coord. Chem. Rev.* **2011**, *255* (7−8), 837−860.
(30) Dinč, M.; Long, J. R. High-Enthalpy Hydrogen Adsorption in Cation-Exchanged Variants of the Microporous Metal−Organic Framework $Mn_3[(Mn_4Cl)_3(BTT)_8(CH_3OH)_{10}]_2$. *J. Am. Chem. Soc.* **2007**, *129* (36), 11172−11176.
(31) Lalonde, M.; Bury, W.; Karagiaridi, O.; Brown, Z.; Hupp, J. T.; Farha, O. K. Transmetalation: Routes to Metal Exchange within Metal−Organic Frameworks. *J. Mater. Chem. A* **2013**, *1* (18), 5453−5468.
(32) Halim, J.; Moon, E. J.; Eklund, P.; Rosen, J.; Barsoum, M. W.; Ouisse, T. Variable Range Hopping and Thermally Activated Transport in Molybdenum-Based MXenes. *Phys. Rev. B* **2018**, *98* (10), 104202.
(33) Neifel'd, E. A.; Arkhipov, V. E.; Ugryumova, N. A.; Korolev, A. V.; Mukovskii, Y. M. Temperature Dependence of the Activation Energy of Manganite Conductivity in the Paramagnetic Phase. *Bull. Russ. Acad. Sci.: Phys.* **2007**, *71* (11), 1559−1560.
(34) Mahjoub, S.; Baazaoui, M.; M'nassri, R.; Boudjada, N. C.; Oumezzine, M. Electrical Conduction and Percolation Model in $Pr_{0.6}Ca_{0.1}Sr_{0.3}Mn_{1-x}Fe_xO_3$ (x = 0, 0.05, and 0.075) Manganites. *J. Supercond. Nov. Magn.* **2015**, *28* (7), 1905−1911.
(35) Misumi, Y.; Yamaguchi, A.; Zhang, Z.; Matsushita, T.; Wada, N.; Tsuchiizu, M.; Awaga, K. Quantum Spin Liquid State in a Two-Dimensional Semiconductive Metal−Organic Framework. *J. Am. Chem. Soc.* **2020**, *142* (39), 16513−16517.
(36) Garreau-de Bonneval, B.; Moineau-Chane Ching, K. I.; Alary, F.; Bui, T.-T.; Valade, L. Neutral d^8 Metal Bis-Dithiolene Complexes: Synthesis, Electronic Properties and Applications. *Coord. Chem. Rev.* **2010**, *254* (13), 1457−1467.
(37) Szilagyi, R. K.; Lim, B. S.; Glaser, T.; Holm, R. H.; Hedman, B.; Hodgson, K. O.; Solomon, E. I. Description of the Ground State Wave Functions of Ni Dithiolenes Using Sulfur K-edge X-ray Absorption Spectroscopy. *J. Am. Chem. Soc.* **2003**, *125* (30), 9158−9169.
(38) Ray, K.; DeBeer George, S.; Solomon, E. I.; Wieghardt, K.; Neese, F. Description of the Ground-State Covalencies of the Bis(dithiolato) Transition-Metal Complexes from X-ray Absorption Spectroscopy and Time-Dependent Density-Functional Calculations. *Eur. J. Chem.* **2007**, *13* (10), 2783−2797.
(39) Krukau, A. V.; Vydrov, O. A.; Izmaylov, A. F.; Scuseria, G. E. Influence of the Exchange Screening Parameter on the Performance of Screened Hybrid Functionals. *J. Chem. Phys.* **2006**, *125*, 224106.
(40) Grimme, S.; Ehrlich, S.; Goerigk, L. Effect of the Damping Function in Dispersion Corrected Density Functional Theory. *J. Comput. Chem.* **2011**, *32* (7), 1456−1465.
(41) Perdew, J. P.; Burke, K.; Ernzerhof, M. Generalized Gradient Approximation Made Simple. *Phys. Rev. Lett.* **1996**, *77* (18), 3865−3868.
(42) Himmetoglu, B.; Floris, A.; de Gironcoli, S.; Cococcioni, M. Hubbard-corrected DFT Energy Functionals: The LDA+U Description of Correlated Systems. *Int. J. Quantum Chem.* **2014**, *114* (1), 14−49.
(43) Sheberla, D.; Bachman, J. C.; Elias, J. S.; Sun, C.-J.; Shao-Horn, Y.; Dincă, M. Conductive MOF Electrodes for Stable Supercapacitors with High Areal Capacitance. *Nat. Mater.* **2017**, *16* (2), 220−224.
(44) Park, J.; Lee, M.; Feng, D.; Huang, Z.; Hinckley, A. C.; Yakovenko, A.; Zou, X.; Cui, Y.; Bao, Z. Stabilization of Hexaaminobenzene in a 2D Conductive Metal−Organic Framework for High Power Sodium Storage. *J. Am. Chem. Soc.* **2018**, *140* (32), 10315−10323.
(45) Nam, K. W.; Park, S. S.; dos Reis, R.; Dravid, V. P.; Kim, H.; Mirkin, C. A.; Stoddart, J. F. Conductive 2D Metal-Organic Framework for High-Performance Cathodes in Aqueous Rechargeable Zinc Batteries. *Nat. Commun.* **2019**, *10* (1), 4948.
(46) Jiang, Q.; Xiong, P.; Liu, J.; Xie, Z.; Wang, Q.; Yang, X.-Q.; Hu, E.; Cao, Y.; Sun, J.; Xu, Y.; et al.et al. A Redox-Active 2D Metal−Organic Framework for Efficient Lithium Storage with Extraordinary High Capacity. *Angew. Chem., Int. Ed.* **2020**, *59* (13), 5273−5277.
(47) Zhang, P.; Wang, M.; Liu, Y.; Yang, S.; Wang, F.; Li, Y.; Chen, G.; Li, Z.; Wang, G.; Zhu, M.; et al.et al. Dual-Redox-Sites Enable Two-Dimensional Conjugated Metal−Organic Frameworks with Large Pseudocapacitance and Wide Potential Window. *J. Am. Chem. Soc.* **2021**, *143* (27), 10168−10176.
(48) Banda, H.; Dou, J.-H.; Chen, T.; Libretto, N. J.; Chaudhary, M.; Bernard, G. M.; Miller, J. T.; Michaelis, V. K.; Dincă, M. High-Capacitance Pseudocapacitors from Li+ Ion Intercalation in Nonporous, Electrically Conductive 2D Coordination Polymers. *J. Am. Chem. Soc.* **2021**, *143* (5), 2285−2292.
(49) Fleischmann, S.; Mitchell, J. B.; Wang, R.; Zhan, C.; Jiang, D.-E.; Presser, V.; Augustyn, V. Pseudocapacitance: From Fundamental Understanding to High Power Energy Storage Materials. *Chem. Rev.* **2020**, *120* (14), 6738−6782.
(50) Morrison, C.; Sun, H.; Yao, Y.; Loomis, R. A.; Buhro, W. E. Methods for the ICP-OES Analysis of Semiconductor Materials. *Chem. Mater.* **2020**, *32* (5), 1760−1768.
(51) Ma, T.; Dong, B. X.; Grocke, G. L.; Strzalka, J.; Patel, S. N. Leveraging Sequential Doping of Semiconducting Polymers to Enable Functionally Graded Materials for Organic Thermoelectrics. *Macromolecules* **2020**, *53* (8), 2882−2892.
(52) Reenen, S. V.; Kemerink, M. Correcting for contact geometry in Seebeck Coefficient Measurements of Thin Film Devices. *Org. Electron.* **2014**, *15* (10), 2250−2255.
(53) Smits, F. M. Measurement of Sheet Resistivities with the Four-Point Probe. *Bell Syst. Technol. J.* **1958**, *37* (3), 711−718.
(54) Bain, G. A.; Berry, J. F. Diamagnetic Corrections and Pascal's Constants. *J. Chem. Educ.* **2008**, *85* (4), 532.
(55) Kresse, G.; Hafner, J. Ab Initio Molecular Dynamics for Liquid Metals. *Phys. Rev. B* **1993**, *47* (1), 558.

https://doi.org/10.1021/jacs.4c01860
J. Am. Chem. Soc. 2024, 146, 12063−12073

(56) Kresse, G.; Furthmüller, J. Efficiency of ab-initio Total Energy Calculations for Metals and Semiconductors Using a Plane-Wave Basis Set. *Comput. Mater. Sci.* **1996**, *6* (1), 15−50.
(57) Kresse, G.; Joubert, D. From Ultrasoft Pseudopotentials to the Projector Augmented-Wave Method. *Phys. Rev. B* **1999**, *59* (3), 1758−1775.

https://doi.org/10.1021/jacs.4c01860
J. Am. Chem. Soc. 2024, 146, 12063−12073